Spontaneous drying of non-polar deep-cavity cavitand pockets in aqueous solution

J. Wesley Barnett,[1] Matthew R. Sullivan,[3] Joshua A. Long,[2] Du Tang,[1] Thong Nguyen,[3] Dor Ben-Amotz,[2] Bruce C. Gibb,[3] Henry S. Ashbaugh[1,*]

[1]Department of Chemical and Biomolecular Engineering, Tulane University, New Orleans, LA 70118

[2]Department of Chemistry, Purdue University, West Lafayette, IN 47907

[3]Department of Chemistry, Tulane University, New Orleans, LA 70118

Henry S. Ashbaugh https://orcid.org/0000-0001-9869-1900

Dor Bern-Amotz https://orcid.org/0000-0003-4683-5401

Bruce C. Gibb https://orcid.org/0000-0002-4478-4084

[*] corresponding author. hanka@tulane.edu

Abstract

There are many open questions regarding the hydration of solvent-exposed, non-polar tracts and pockets in proteins. Although water is predicted to de-wet purely repulsive surfaces and evacuate crevices, the extent of de-wetting is unclear when ubiquitous van der Waals interactions are in play. The structural simplicity of synthetic supramolecular hosts imbues them with considerable potential to address this issue. To this end, here we detail a combination of densimetry and molecular dynamics simulations of three cavitands, coupled with calorimetric studies of their complexes with short-chain carboxylates. Our results reveal the range of wettability possible within the ostensibly identical cavitand pockets — which differ only in the presence/position of the methyl groups that encircle the portal to their non-polar pockets. The results demonstrate the ability of macrocycles to template water cavitation within their binding sites and show how the orientation of methyl groups can trigger the drying of non-polar pockets in liquid water, suggesting new avenues to control guest complexation.

While *horror vacui*, Aristotle's philosophical position that nature abhors a vacuum, may be viewed as self-evident, a more considered thermodynamic analysis of the stability of confined liquids challenges this intuition. In particular, water is predicted to pull away from and de-wet idealized (purely-repulsive) large non-polar solutes,[1-3] and to evacuate slits and crevices with dimensions smaller than a context dependent "drying" lengthscale.[4-6] Ubiquitous attractive van der Waals interactions, however, temper de-wetting, making experimental detection of drying exceedingly challenging.[2, 7-12] While the full implications of hydrophobic de-wetting phenomena are not yet clear, its potential biological relevance is exemplified by experimental and theoretical results indicating that the non-polar cavities of some proteins remain dry when dissolved in liquid water;[5, 6, 13-15] although this is not an entirely settled question.[4, 14, 16, 17] Here, using a combination of densimetry, calorimetry, and molecular dynamics (MD) simulations, we reveal direct evidence of wetting/de-wetting of the binding sites of three deep-cavity cavitand hosts. These hosts possess very similar non-polar pockets (Figure 1), but the hydration of their binding sites is subtly controlled by the position of methyl groups encircling the portal to their non-polar pockets. This ability to engineer the wetting properties of molecular pockets, and the resultant solvent-mediated interactions between host and guest species, opens new routes for modulating binding affinities.

High-pressure X-ray crystallography and MD simulations of T4 lysozyme provided some of the first evidence that non-polar protein cavities exhibit a drying transition.[5] Specifically, the relatively large (~160 Å^3), rigid hydrophobic cavity of the L99A mutant was found to be empty at ambient pressure and to cooperatively fill with water at elevated pressures, suggesting a mechanism for pressure denaturation. Subsequent NMR and MD studies indicated that the substantially larger (~315 Å^3) ligand-binding pocket of bovine β-lactoglobulin is largely dry in water with only transient (sub-nanosecond) filling events.[6] Such cavity de-wetting is expected to impact the binding kinetics and thermodynamics of fatty acid ligands to this apoprotein. Indeed, recent experimental[18, 19] and simulation[20] studies have emphasized that binding to protein pockets, synthetic hosts,[21, 22] and non-polar

depressions can be dominated by favorable enthalpic contributions. This "non-classical hydrophobic effect" is in contrast to the classic interpretation ascribing favorable hydrophobic association to the entropic release of structured waters from oily surfaces.[23] The difficulties associated with experimentally identifying dry cavities, however, is exemplified by apparently conflicting NMR[16] and X-ray[17] evidence pertaining to the relatively small (~80 Å^3) cavity of interleukin-1β, although MD simulations support X-ray results implying the cavity is dry at ambient conditions.[14]

Figure 1 illustrates the structures of the three cavitand hosts whose cavity hydration we have investigated both experimentally and theoretically: Octa-acid (OA, **1**), tetra-*endo*-methyl octa-acid (TEMOA, **2**), and tetra-*exo*-methyl octa-acid (TEXMOA, **3**). As shown in Figure 1b, each host is truly concave; the cavity is closed off at its base to form a bowl-like binding site. In each case the cavity is ~8-9 Å deep, and ~8 Å wide at the portal (volume ~260 Å^3, Supporting Table 6). TEMOA **2** differs from OA **1** by possessing four methyl groups that project from the rim of the host and narrow the portal slightly at four points. These do not represent a direct steric barrier to egression[24] or entry for water and most guests. Thus, only in the case of highly rotund and rigid guests, *e.g.*, adamantyl derivatives, do these methyl groups affect the kinetics and thermodynamics of guest binding.[25] Moving the methyl groups from the *endo*-position (TEMOA **2**) to the *exo*-position leads to the constitutional isomer TEXMOA **3**. Here the methyl groups point upwards, crenellating the pocket rim but otherwise leaving the binding site essentially identical to that of OA **1**.

The parent OA **1**[26, 27] and its methylated derivative TEMOA **2** have been reported previously.[28, 29] TEXMOA **3**, the synthesis of which is described in the Supporting Information, has not been previously reported. Driven by the hydrophobic effect, both hosts **1** and **2** can assemble into supramolecular capsules.[30] However, they also form 1:1 host-guest complexes with guests that render the portal region hydrophilic.[25, 31-35] Thus, amphiphiles such as short chain fatty acids, as well as relatively large, polarizable anions such as perchlorate, form

1:1 complexes. For both kinds of guests, binding has been characterized thermodynamically using Isothermal Titration Calorimetry (ITC).[25, 31-35]

Here we consider how the non-polar pocket hydration of hosts **1**–**3** changes with the orientation of the methyl groups encircling the portal, with an eye towards determining signatures of drying of the pocket. Changes in the hydration state are characterized through high-precision densimetry experiments which provide evidence of water packing about the hosts, ITC which gives thermodynamic information on guest binding, and MD simulations which yield molecular resolution on the hydration of non-polar host surfaces. These results represent the first identification of drying in a wholly synthetic host, opening up routes for the precise modulation of guest binding/recognition in water.

Results and Discussion

Volumes of hydrated cavitands. Figure 2 displays the measured inverse densities of solutions of the three cavitands as a function of the cavitand mass fraction, w. The host partial molar volumes at infinite dilution, $\overline{v}$, were obtained using the thermodynamic expression:

$$\overline{v} = M\left(\frac{1}{\rho_0} + S_0\right), \qquad [1]$$

where M is the cavitand molar mass, ρ_0 is the density of the solvent (pertaining to the pH = 12.7±0.2 aqueous sodium hydroxide solutions used), and S_0 is the initial slope of $1/\rho$ with respect to w. The data in Figure 2 can be treated as linear functions over the range of host mass fractions considered, permitting S_0 determination by linear regression (Figure 2 and Supporting Figure 16).

Table 1 contains the experimental host partial molar volumes and volume differences, $\Delta\overline{v}_{ij} = \overline{v}_i - \overline{v}_j$, for hosts i and j. Note that the experimental results reflect both the volume of the anionic cavitand and volume change due to the conversion of OH^- to H_2O upon host ionization. However, assuming all the cavitands have the same degree of ionization, the differences between the measured partial molar volumes are equivalent to the corresponding host volume differences. Strikingly, the impact of host methylation on the measured volume differences strongly depends on their placement about the portal. The volume

difference between hosts **3** and **1** is 73±7 cm^3/mol, closely corresponding to the volumes of the four added methyl groups. For comparison, the volume difference between alanine and glycine amino acid side chains is 18.3 cm^3/mol,[36] which is one fourth of $\Delta\overline{v}_{\mathbf{31}}$. In contrast, the volume difference between **2** and **1** is 162±12 cm^3/mol, anomalously more than twice the increment associated with adding four methyl groups. A salient conclusion is that the apparent volume of **2** is significantly larger than its actual physical size, revealing the additional volume increase associated with water's exclusion from the pocket of **2** (*vide infra*).

The simulation results provided in Table 1 and Figure 3 provide a molecular-level rationale for the densimetry experiments above based on the hydration behavior of hosts **1**–**3**. The predicted partial molar volumes given in Table 1 are in remarkably good agreement with experiment, differing at most by 2%. More importantly, the simulations capture the anomalous experimental volume differences. Specifically, the simulated partial molar volume difference between hosts **3** and **1** is 81± 3 cm^3/mol (Table 1), closely corresponding to the volume of the four methyl groups, while the simulated volume difference between hosts **2** and **1** is 148±3 cm^3/mol, significantly greater than that of the methyl groups and comparable to the experimental increment.

More revealingly, Figure 3a reports the equilibrium probability distribution of waters within each host pocket. For host **1**, the pocket hydration distribution is nearly unimodal with a single dominant peak centered near n = 4 waters within the pocket. The hydration distributions of both **1** and **3** are slightly asymmetric (non-Gaussian). With increasing numbers of waters, the probability falls to zero for $n \gtrsim$ 8, while for low hydration numbers the tail tends towards a second, weak maximum so that the probability of observing an empty pocket is ~5% $(= p_{\mathbf{1}}(0))$. The simulations also reveal that the pocket hydration distribution of host **3** is practically identical to that of **1**, indicating that the four *exo*-methyl groups do not significantly alter the pocket's hydration statistics. The hydration number distribution of host **2**, however, dramatically differs from that of either **1** or **3**.[15] In particular, the bimodal nature of the hydration distribution of **2** is more apparent with clear peaks at both $n = 0$ and 3. Notably, the pocket of host **2** is empty ~73% $(= p_{\mathbf{2}}(0))$ of the time.

Thus, these results indicate that repositioning the methyl groups from the upward-pointing *exo*-positions to the inward-pointing *endo*-positions dramatically alters pocket hydration. These changes in the hydration distribution are reflected in the mean pocket hydration numbers of ~3.5 for **1** and **3** and 0.74 for **2** (Supporting Table 2).

Our MD results further reveal that the inward pointing *endo*-methyls of **2** do not significantly alter the pocket shape, as confirmed by the fact that the hydration statistics of **2** are essentially identical to hosts **1** and **3** at high pressure (Supporting Figure 21). The resulting volume difference between **1** and **2** is 73 cm^3/mol at 2500 bar, which is identical to that between **1** and **3**, corresponding to the volume of the added methyl groups (Supporting Table 4). Moreover, the van der Waals volumes of the host pockets calculated *in vacuo* are practically indistinguishable from one another (Supporting Table 6).

One way to view host drying is through the lens of capillary evaporation of confined non-polar surfaces. At ambient pressure, the hydration distributions of each host arise from the free energy difference between their filled and empty states (Wet/dry host water distributions imaged in Supporting Figure 20). Following a macroscopic perspective, the free energy for filling the pocket is expected to be proportional to the surface area of the pocket (with the constant of proportionality equated with a solid/water interfacial tension), relative to the free energy for creating an air/water interface across the portal (accompanied with a corresponding air/water interfacial tension).[2, 37] A larger tension of the air/water interface favors wet states, while a larger surface area of the pocket compared to that across the portal favors dry states. Considering the hydration number distributions for **1** and **3** the system regularly visits the wet and dry states (Figure 3a), with the pocket empty nearly 5% of the time. Moving the methyl groups from the *exo*- to *endo*-positions partially narrows the portal, thus decreasing the area of the opening, without changing the volume of the cavity and so tipping the hydration distribution of **2** from wet to dry. While the application of macroscopic tensions down to sub-nanometer dimensions is questionable, simulations of the wetting of molecular-sized slits have shown the macroscopic thermodynamic framework is

quantitatively accurate if effective interfacial tensions are used.[37] The validity of this capillary evaporation proposition is more clearly illustrated in the pressure dependence of the hydration number distribution for host **2**, which exhibits a bimodal distribution between wet and dry states separated by a free energy barrier at $n = 1$ (Supporting Figure 22).

The influence of hydration on host volumes can be further scrutinized by considering the dependence of the partial molar volume on the pocket hydration number (Figure 3b). As might be intuitively expected, the host partial molar volumes are decreasing functions of the pocket hydration number; that is the hosts appear smaller as water fills their pockets. More interestingly, the volumes of **2** and **3** as a function of the hydration number are essentially the same, indicating the volumetric differences between **2** and **3** are not the result of intrinsic differences in water packing. Moreover, the volume distributions for **2** and **3** appear shifted upwards from that of **1** by 81 cm^3/mol (Figure 3b), corresponding to the simulated $\Delta\overline{v}_{\mathbf{31}}$ reported in Table 1. In other words, the primary differences between the hydration number dependent volumes of **1**, **2**, and **3** is the physical volume of the methyl groups. Thus, the anomalously large partial molar volume of **2** is a result of weighting of the mean volume towards dry states by its hydration number distribution (Figure 3) compared to the relatively wet **3**. Restated, the anomalously large volume of host **2** over **3** is a macroscopic signature of nanoscale de-wetting of its pocket.

Comparing the experimental versus simulated volume differences between **2** and either **1** or **3** (Table 1), it appears the experimental increments are slightly greater than the MD predictions. If the simulated pocket of **2** was completely empty (*i.e.*, $\langle n \rangle = 0$, with $p_{\mathbf{2}}(0) = 1$ and $p_{\mathbf{2}}(n > 0) = 0$), however, we predict the volume of **2** would be 1,278±5 cm^3/mol. The resultant volume difference is $\Delta\overline{v}_{\mathbf{21}} = 170\pm3$ cm^3/mol, slightly greater than the experimental difference. Thus, our experiments suggest that the pocket of **2** is actually dryer than predicted from simulation.

Role of drying on guest binding. A rational question that follows from this observed cavity drying is; what is its impact on host-guest binding? To investigate this, we used ITC to explore the thermodynamics of binding of select *n*-alkyl

carboxylates to highly hydrated host **1** and poorly hydrated **2**. ITC directly provides the enthalpy of complexation (ΔH), and yields the free energy (ΔG), entropy ($-T\Delta S$), and heat capacity (ΔC_P) (Table 3, Supporting Figures 24-33, and Supporting Tables 7 and 8). Table 2 reveals the binding affinity increases with increasing guest length for both hosts. Moreover, in all cases guest binding is stronger to host **2** than to host **1**, with binding to **2** always more exothermic and more entropically penalized. Typically, binding events that are exothermic and entropically penalized are descried as involving the, "non-classical hydrophobic effect" (despite the fact that the temperature and guest size dependence of the hydrophobic effect makes such terms of limited utility; see Supporting Tables 7 and 8).[38] Table 3 also shows that binding to both hosts involves a typical drop in the system heat capacity. Interestingly (*vide infra*), there is a greater heat capacity loss when guests bind to **2** ($\langle\Delta\Delta C_P\rangle = -28.8$ cal/(mol·K) across all guests).

To investigate the source of these differences, we used simulations to evaluate the thermodynamics of water evacuation from the host pockets. Figure 4 reports the drying free energies of hosts **1**–**3** as a function of temperature, evaluated from the pocket hydration number distributions as $\Delta G_{dry} = -kTlnp(0)$. While ΔG_{dry} for evacuating **1** and **3** are comparable, the penalty for drying **2** is significantly lower. The apparent linear dependence of ΔG_{dry} on temperature permits extraction of drying enthalpies and entropies (*i.e.*, $\Delta G_{dry} = \Delta H_{dry} - T\Delta S_{dry}$, where ΔH_{dry} and $T\Delta S_{dry}$ are temperature independent). Drying of **1** and **3** is enthalpically unfavorable and entropically favorable (Table 4), with close agreement between their enthalpies and entropies. On the other hand, the drying enthalpy and entropy of **2** are smaller by an order of magnitude (consistent with there being fewer waters in **2**). Interestingly, despite the fact water loses hydrogen-bonds within the pocket (Supporting Figure 23), the results in Table 3 indicate water is enthalpically stabilized inside a wet host, due to the combined influence of attractive van der Waals interactions with the wet host and loss of hydrogen-bonding for interfacial waters at the portal of a dry host. The latter contribution evidently dominates as the signs of the drying enthalpy and entropy of **1** and **3** are consistent with those associated with creating a macroscopic air/water interface.

The signs and magnitudes of the thermodynamic property differences reported in Table 3 are in excellent agreement with the experimental host-guest binding data from Table 2. Taken together, our results suggest that the weaker, less exothermic, and less entropically penalized guest complexation to host **1** is a result of its higher water occupancy. The strongest interactions between any two molecules occurs *in vacuo*, and in the case of **2**, the absence of water from the pocket facilitates stronger guest binding. In the parlance of supramolecular chemistry, water is the weakest of guests for host **2**, and its absence means that the fatty acid guests do not have to compete with it for binding. As previously noted,[35] hosts such as **2** promote (template) cavity formation in water; their structural preorganization prepays the normally high energetic costs of cavity formation. We believe this may lie behind, for example, the frequently observed strong binding of guests to cucurbiturils.[39, 40]

The greater ΔC_P loss upon guest binding to **2** versus **1** (Table 2) is consistent with the greater energetic fluctuations of water at the air/water interface across the portal of **2**. Guest binding would remove these interfacial fluctuations leading to a larger heat capacity drop. Alternatively, the negative $\Delta\Delta C_P$ could result from the guest displacing waters from the bulk facing side of the *endo*-methyl groups of **2**. However, more work is needed to discriminate between these or alternative scenarios.

In conclusion, our experimental and simulation results provide direct evidence of the de-wetting of a synthetic, non-biological host in water. De-wetting is triggered by the position of methyl groups encircling the non-polar pocket; in their absence (**1**), or when the methyl groups are pointed “upwards” (**3**), the pocket is found to be wet. In contrast, when the rim methyl groups are positioned "inward" near the pocket portal (**2**), water evacuates the pocket in a manner analogous to capillary evaporation. We find that de-wetting of **2** leads to an increased guest affinity that is enthalpically more favored and entropically less favorable. Thus, from a supramolecular perspective, water is a poorer guest for **2** and cannot effectively compete for the pocket; hence (organic) guest binding is enhanced. This graphic example of the “non-classical hydrophobic effect” emphasizes the

dependence of the hydrophobic effect on subtle surface shape differences.[15, 41] Our results also suggest a new perspective regarding water's role in non-polar host cavities.[21, 22] Thus whether a pocket is wet or dry depends on the balance between attractive van der Waals interactions and limited hydrogen-bonding within the host, against the consequences of establishing an air/water interface at the threshold. When the balance is shifted to the dry state, guest complexation is enhanced because of reduced competition with water. These results highlight a new route to designer guest affinities by manipulation of host cavity wetting propensities.

References

1. Stillinger, F. H. Structure in aqueous solutions of nonpolar solutes from the standpoint of scaled-particle theory. *J. Soln. Chem.* **2**, 141-158 (1973).

2. Chandler, D. Interfaces and the driving force of hydrophobic assembly. *Nature* **437**, 640-647 (2005).

3. Ashbaugh, H. S. & Pratt L. R. Colloquium: Scaled particle theory and the length scales of hydrophobicity. *Rev. Mod. Phys.* **78**, 159-178 (2006).

4. Rasaiah, J. C., Garde S. & Hummer G. Water in nonpolar confinement: From nanotubes to proteins and beyond. *Ann. Rev. Phys. Chem.* **59**, 713-740 (2008).

5. Collins, M. D., Hummer G., Quillin M. L., Matthews B. W. & Gruner S. M. Cooperative water filling of a nonpolar protein cavity observed by high-pressure crystallography and simulation. *Proc. Natl. Acad. Sci. USA* **102**, 16668-16671 (2005).

6. Qvist, J., Davidovic M., Hamelberg D. & Halle B. A dry ligand-binding cavity in a solvated protein. *Proc. Natl. Acad. Sci. USA* **105**, 6296-6301 (2008).

7. Hummer, G., Rasaiah J. C. & Noworyta J. P. Water conduction through the hydrophobic channel of a carbon nanotube. *Nature* **414**, 188-190 (2001).

8. Huang, D. M. & Chandler D. The hydrophobic effect and the influence of solute-solvent attractions. *J. Phys. Chem. B* **106**, 2047-2053 (2002).

9. Ben-Amotz, D. Water-mediated hydrophobic interactions. *Ann. Rev. Phys. Chem.* **67**, 617-638 (2016).

10. Li, I. T. S. & Walker G. C. Signature of hydrophobic hydration in a single polymer. *Proc. Natl. Acad. Sci. USA* **108**, 16527-16532 (2011).

11. Davis, J. G., Gierszal K. P., Wang P. & Ben-Amotz D. Water structural transformation at molecular hydrophobic interfaces. *Nature* **491**, 582-585 (2012).

12. Wu, X. G., Lu W. J., Streacker L. M., Ashbaugh H. S. & Ben-Amotz D. Temperature-dependent hydrophobic crossover length scale and water tetrahedral order. *J. Phys. Chem. Lett.* **9**, 1012-1017 (2018).

13. Collins, M. D., Quillin M. L., Hummer G., Matthews B. W. & Gruner S. M. Structural rigidity of a large cavity-containing protein revealed by high-pressure crystallography. *J. Molec. Bio.* **367**, 752-763 (2007).

14. Yin, H., Feng G. G., Clore G. M., Hummer G. & Rasaiah J. C. Water in the polar and nonpolar cavities of the protein interleukin-1 beta. *J. Phys. Chem. B* **114**, 16290-16297 (2010).

15. Patel, A. J., Varilly P., Jamadagni S. N., Hagan M. F., Chandler D. & Garde S. Sitting at the edge: How biomolecules use hydrophobicity to tune their interactions and function. *J. Phys. Chem. B* **116**, 2498-2503 (2012).

16. Ernst, J. A., Clubb R. T., Zhou H. X., Gronenborn A. M. & Clore G. M. Demonstration of positionally disordered water within a protein hydrophobic cavity by NMR. *Science* **267**, 1813-1817 (1995).

17. Finzel, B. C., Clancy L. L., Holland D. R., Muchmore S. W., Watenpaugh K. D. & Einspahr H. M. Crystal-structure of recombinant human interleukin-1-beta at 2.0-Å resolution. *J. Molec. Bio.* **209**, 779-791 (1989).

18. Snyder, P. W., Mecinovic J., Moustakas D. T., Thomas S. W., Harder M., Mack E. T., Lockett M. R., Heroux A., Sherman W. & Whitesides G. M. Mechanism of the hydrophobic effect in the biomolecular recognition of arylsulfonamides by carbonic anhydrase. *Proc. Natl. Acad. Sci. USA* **108**, 17889-17894 (2011).

19. Myslinski, J. M., DeLorbe J. E., Clements J. H. & Martin S. F. Protein-ligand interactions: Thermodynamic effects associated with increasing nonpolar surface area. *J. Am. Chem. Soc.* **133**, 18518-18521 (2011).

20. Setny, P., Baron R. & McCammon J. A. How can hydrophobic association be enthalpy driven? *J. Chem. Theo. Comput.* **6**, 2866-2871 (2010).

21. Biedermann, F., Vendruscolo M., Scherman O. A., De Simone A. & Nau W. M. Cucurbit 8 uril and Blue-Box: High-energy water release overwhelms electrostatic interactions. *J. Am. Chem. Soc.* **135**, 14879-14888 (2013).

22. Biedermann, F., Nau W. M. & Schneider H. J. The hydrophobic effect revisited-studies with supramolecular complexes imply high-energy water as a noncovalent driving force. *Angew. Chem.-Int. Edit.* **53**, 11158-11171 (2014).

23. Hummer, G. Molecular binding: Under water's influence. *Nat. Chem.* **2**, 906-907 (2010).

24. Giri, N., Del Pópolo M. G., Melaugh G., Greenway R. L., Rätzke K., Koschine T., Pison L., Costa Gomes M. F., Cooper A. I. & James S. L. Liquids with permanent porosity. *Nature* **527**, 216-220 (2015).

25. Sullivan, M. R., Sokkalingam P., Nguyen T., Donahue J. P. & Gibb B. C. Binding of carboxylate and trimethylammonium salts to octa-acid and TEMOA deep-cavity cavitands. *J. Comp.-Aided Molec. Des.* **31**, 21-28 (2017).

26. Gibb, C. L. D. & Gibb B. C. Well-defined, organic nanoenvironments in water: The hydrophobic effect drives a capsular assembly. *J. Am. Chem. Soc.* **126**, 11408-11409 (2004).

27. Liu, S. M., Whisenhunt-Ioup S. E., Gibb C. L. D. & Gibb B. C. An improved synthesis of 'octa-acid' deep-cavity cavitand. *Supramol. Chem.* **23**, 480-485 (2011).

28. Gan, H. Y., Benjamin C. J. & Gibb B. C. Nonmonotonic assembly of a deep-cavity cavitand. *J. Am. Chem. Soc.* **133**, 4770-4773 (2011).

29. Gan, H. Y. & Gibb B. C. Guest-mediated switching of the assembly state of a water-soluble deep-cavity cavitand. *Chem. Commun.* **49**, 1395-1397 (2013).

30. Jordan, J. H. & Gibb B. C. Molecular containers assembled through the hydrophobic effect. *Chem. Soc. Rev.* **44**, 547-585 (2015).

31. Gibb, C. L. D. & Gibb B. C. Binding of cyclic carboxylates to octa-acid deep-cavity cavitand. *J. Comp.-Aided Molec. Des.* **28**, 319-325 (2014).

32. Gibb, C. L. D. & Gibb B. C. Anion binding to hydrophobic concavity Is central to the salting-in effects of Hofmeister chaotropes. *J. Am. Chem. Soc.* **133**, 7344-7347 (2011).

33. Carnegie, R. S., Gibb C. L. D. & Gibb B. C. Anion complexation and the hofmeister effect. *Angew. Chem.-Int. Edit.* **53**, 11498-11500 (2014).

34. Sokkalingam, P., Shraberg J., Rick S. W. & Gibb B. C. Binding hydrated anions with hydrophobic pockets. *J. Am. Chem. Soc.* **138**, 48-51 (2016).

35. Sullivan, M. R., Yao W., Tang D., Ashbaugh H. S. & Gibb B. C. The thermodynamics of anion complexation to nonpolar pockets. *J. Phys. Chem. B* **122**, 1702-1713 (2018).

36. Hedwig, G. R. & Hinz H. J. Group additivity schemes for the calculation of the partial molar heat capacities and volumes of unfolded proteins in aqueous solution. *Biophys. Chem.* **100**, 239-260 (2003).

37. Ashbaugh, H. S. Solvent cavitation under solvophobic confinement. *J. Chem. Phys.* **139**, 064702 (2013).

38. Cremer, P. S., Flood A. H., Gibb B. C. & Mobley D. L. Collaborative routes to clarifying the murky waters of aqueous supramolecular chemistry. *Nat. Chem.* **10**, 8-16 (2018).

39. Cao, L. P., Sekutor M., Zavalij P. Y., Mlinaric-Majerski K., Glaser R. & Isaacs L. Cucurbit 7 uril.guest pair with an attomolar dissociation constant. *Angew. Chem.-Int. Edit.* **53**, 988-993 (2014).

40. Assaf, K. I. & Nau W. M. Cucurbiturils: From synthesis to high-affinity binding and catalysis. *Chem. Soc. Rev.* **44**, 394-418 (2015).

41. Hillyer, M. B. & Gibb B. C. Molecular shape and hydrophobic effect. *Ann. Rev. Phys. Chem.* **67**, 307-329 (2016).

Acknowledgements

MRS, TN, and BCG would like to acknowledge the National Institutes of Health (GM125690) and the National Science Foundation (CHE–1807101) for financial support. BCG and HSA gratefully acknowledge the support of the National Science Foundation (CBET–1403167 and CBET–1805167). JAL and DBA gratefully acknowledge support from the National Science Foundation (CHE–1763581). JWB gratefully acknowledges financial support from the Louisiana Board of Regents. JWB, DT, and HSA thank the Louisiana Optical Network Initiative who provided computational support.

Author Contributions

JWB, DT, MRS and JAL contributed equally to this publication. JWB and DT performed the molecular simulations of the cavitands in water. MRS carried out the described guest-binding thermodynamic determinations with ITC. JAL carried out all of the described partial molar volume measurements on hosts **1**–**3**. TN synthesized TEXMOA (**3**). DBA, BCG, and HSA conceived and directed the research and contributed to the data analysis and manuscript preparation.

Competing Interests

The authors declare no competing interests.

Figure Legends

Fig. 1| Chemical structures and illustrations of the deep-cavity cavitand hosts examined. This figure demonstrates the relative positioning of the methyl groups encircling the portal of hosts **2** and **3** that can trigger de-wetting of their non-polar binding pockets. (**a**) Chemical structures of octa-acid (OA, **1**), tetra-*endo*-methyl octa-acid (TEMOA, **2**), and tetra-*exo*-methyl octa-acid (TEXMOA), **3**); (**b**) Space-filling representations of **1**, **2** and **3** showing the structural differences of adding methyl groups (colored pink) to the *endo*-position (**2**) and *exo*-position (**3**) of the non-polar pocket.

Fig. 2| Determination of cavitand volumes by measurement of densities of hosts in aqueous solution. The results in this figure demonstrate host **2** is substantially larger than either hosts **1** or **3** in aqueous solution, providing experimental evidence of de-wetting of host **2**'s non-polar pocket. Inverse of the experimentally determined solution density plotted as a function of the host mass fraction at 25°C. The symbols for hosts **1**–**3** are identified in the legend. The lines indicate linear fits to the experimental data. Error bars in the mass fraction and density indicate one standard deviation.

Fig. 3| Molecular simulation characterization of cavitand pocket hydration and volume. These figures characterize the hydration state of the non-polar pockets of hosts **1**–**3** and the role of de-wetting on determining their partial molecular volumes. (**a**) Hydration number probability distribution, $p(n)$, as a function of the number of waters within the cavitand's non-polar pocket, n, determined from simulations at 25 °C and 1 bar. The symbols for hosts **1**–**3** are identified in the figure legend. (**b**) Cavitand partial molar volumes, $\overline{v}(n)$, as a function of the number of hydration waters in the non-polar pocket determined from simulation. The macroscopic partial molar host volume is determined by the weighted average $\overline{v} = \sum p(n)\overline{v}(n)$. The symbols correspond to results for **1**, **2**, and **3** as defined in (**a**)**.** The thick, dashed, red line corresponds to the results for **1**

shifted up by Δ = 81 cm^3/mol. The error bars in both figures indicate one standard deviation.

Fig. 4| Molecular simulation evaluation of cavitand pocket drying thermodynamics. The results in this figure enable evaluation of the enthalpic and entropic contributions to cavitand pocket de-wetting, enabling assessment of the role of de-wetting on guest binding. Free energy of drying ($G_{dry} = -kTlnp(0)$) hosts **1**–**3** as a function of temperature determined from simulation. The symbols for hosts **1**–**3** are identified in the figure legend. The lines indicate fits of the drying free energies to the expression $\Delta G_{dry} = \Delta H_{dry} - T\Delta S_{dry}$, assuming the enthalpy and entropy are constant. The error bars indicate one standard deviation.

Tables

Table 1| Volumetric properties of host in aqueous solution from experiment and simulation. Cavitand partial molar volumes, $\overline{v}_i$, and partial molar volume differences, $\Delta\overline{v}_{ij} = \overline{v}_i - \overline{v}_j$, from experiment and MD simulation at 25°C and ambient pressure. Experimental partial molar volumes were obtained from the average of two independently prepared samples, with the reported error representing the maximum deviation from the average represent the simulation errors indicate one stand deviation.

	$\overline{v}_1$ (cm^3/mol)	$\overline{v}_2$ (cm^3/mol)	$\overline{v}_3$ (cm^3/mol)	$\Delta\overline{v}_{31}$ (cm^3/mol)	$\Delta\overline{v}_{21}$ (cm^3/mol)	$\Delta\overline{v}_{23}$ (cm^3/mol)
experiment	1083±3	1245±12	1157±6	73±7	162±12	89±13
simulation	1108±5	1256±5	1189±5	81±3	148±3	67±2

Table 2| Thermodynamics of guest binding to "wet" and "dry" hosts. Thermodynamics for the complexation of fatty acid to hosts **1** and **2** at 25°C and their corresponding differences. Errors (typically < 10%) are provided in the SI.

Host 1

Guest	K_a (M^{-1})	ΔG (kcal/mol)	ΔH (kcal/mol)	$-T\Delta S$ (kcal/mol)	ΔC_P (cal/mol K)
hexanoate	6.05×10^3	–5.16	–5.74	0.59	-68.3
heptanoate	3.80×10^4	–6.24	–6.49	0.24	-89.0
octanoate	1.37×10^5	–7.00	–6.12	–0.89	–115.6
nonanoate	3.37×10^5	–7.54	–6.46	–1.08	–133.3
decanoate	6.33×10^5	–7.91	–6.48	–1.43	–154.5

Host 2

Guest	K_a (M^{-1})	ΔG (kcal/mol)	ΔH (kcal/mol)	$-T\Delta S$ (kcal/mol)	ΔC_P (cal/mol·K)
hexanoate	2.70×10^4	–6.04	–7.53	1.49	–95.1
heptanoate	2.35×10^5	–7.32	–8.54	1.21	–119.3
octanoate	1.49×10^6	–8.42	–8.69	0.27	–143.3
nonanoate	3.51×10^6	–8.92	–9.67	0.75	–164.9
decanoate	4.40×10^6	–9.05	–9.08	0.03	–182.1

Difference (2 – 1)

Guest	K_a (M^{-1})	$\Delta\Delta G$ (kcal/mol)	$\Delta\Delta H$ (kcal/mol)	$-T\Delta\Delta S$ (kcal/mol)	$\Delta\Delta C_P$ (cal/mol·K)
hexanoate	--	–0.88	–1.79	0.90	–26.8
heptanoate	--	–1.08	–2.05	0.97	–30.3
octanoate	--	–1.42	–2.57	1.16	–27.7
nonanoate	--	–1.38	–3.21	1.83	–31.6
decanoate	--	–1.14	–2.60	1.46	–27.6

Table 3| Thermodynamics of host drying. Cavitand drying free energies, enthalpies, and entropies at 25°C as determined from linear fits of simulation drying free energies (Figure 4). Thermodynamic properties reported in groups of kcal/mol. Errors indicate one standard deviation

	1	**2**	**3**	**2 - 1**	**3 - 1**
ΔG_{dry}	1.90±0.02	0.21±0.02	1.74±0.01	-1.69±0.03	-0.16±0.03
ΔH_{dry}	3.86±0.20	0.13±0.18	3.53±0.09	-3.73±0.27	-0.33±0.26
$-T\Delta S_{dry}$	-1.96±0.18	0.08±0.16	-1.79±0.08	2.04±0.24	0.17±0.23

Methods

Synthesis and characterization of tetra-exo-methyl octa-acid. Full experimental details, procedures, and characterization for the newly synthesized cavitand (TEXMOA **3**) are provided in Section 1 of the Supporting Information.

Partial molar volume measurement. Density measurements were made with a vibrating U-tube densimeter (Anton-Paar DSA 5000), using sample volumes ≥ 2.5 mL. The densimeter was cleaned as specified by the manufacturer and calibrated using degassed water and dry air. To obtain partial molar volumes at infinite dilution ($\overline{v}$), multiple concentrations between ~0.2% (w/w) and 1% (w/w) were used. The uncertainty in density measurements was 5×10^{-6} g/cm^3, as obtained from replicate measurements of pure water. The uncertainty of the weight percent values was 0.02% (w/w), as obtained from the error in the slope of the inverse density as a function of weight percent in four independent replicate sample preparations and measurements of aqueous TEMOA solutions at 25ºC.

Sodium hydroxide (98.5%, Acros Organics) was used without further purification. Aqueous solutions were prepared using ultrapure water (Milli-Q UF Plus, 18.2 MΩ·cm, Millipore), which was degassed by boiling for at least 15 minutes. For each set of measurements, a sodium hydroxide solution with pH 12.7±0.2 was prepared as the host solvent. The cavitands were dissolved in solution at concentrations from 0 to ~0.7% (w/w). The pH of each solution was measured using a Pinnacle 530 pH meter (Corning).

To determine the partial molar volumes of cavitand hosts, the reciprocal of the measure solution density ($1/\rho$ in cm^3/g) was plotted as a function of the host mass fractions (w). From this plot, the slope S_0 (cm^3/g) through the data was determined by linear regression and the partial molar volumes were evaluated following eq. [1].

Since the solid cavitands are protonated acids (rather than salts) the observed density changes arise both from the partial molar volume of the ionized cavitand and the volume change associated with converting $OH^-_{(aq)}$ to H_2O upon deprotonation of the cavitand.

Additional information on the densimetry experiments is provided in Section 2 of the Supporting Information.

Molecular simulation details. Molecular Dynamics (MD) simulations of cavitands in water were conducted using GROMACS 5.1.[42] Water was modeled using the TIP4P/EW potential.[43] The cavitands and sodium counterions were modeled using the Generalized Amber Force Field (GAFF).[44] No salt beyond the explicit counterions were included in the simulations. Cavitand partial charges were assigned using AM1-BCC[45] calculations following geometry optimization. The net cavitand charge was assumed to be -6e at pH 7, neutralized by 6 sodium counterions modeled using GAFF.[46] The four acidic coating groups ringing the hydrophobic pocket at the top of OA and two acids diagonal to one another at the foot of OA were deprotonated (Figure S12). Charges on the hosts and their counterions were scaled to 75% of their full value to account for polarization effects. This does not impact the physics of cavitand de-wetting as discussed in the Supporting Information. Simulations were performed at 25 °C and 1 bar with periodic boundary conditions. Long-range electrostatics were evaluated using particle-mesh Ewald summation,[47] while a 9 Å cut-off was implemented for non-bonded interactions. Simulations were performed in the isothermal-isobaric ensemble at 25˚C and pressures from 1 to 2500 bar. The temperature and pressure were controlled using the Nosé-Hoover thermostat[48, 49] and Parrinello-Rahman barostat,[50] respectively. Bonds involving hydrogens for the hosts and guests were constrained using the LINCS algorithm,[51] while water was held rigid using SETTLE.[52] Cavitands were hydrated with 2000 waters, while simulations of 2184 waters were conducted to determine pure water properties. Production runs were conducted for 200 ns following at least 1 ns for equilibration. The equations of motion were integrated using a 2 fs time step. Simulation configurations were saved every 1 ps for analysis. GROMACS topology (.top) and Gromos87 (.gro) files for hosts **1** – **3** are provided in the **Supporting Data**.

To determine the number of waters within a cavitand and their van der Waals volumes a hexahedron was constructed from the atoms making up the

cavitand (Supporting Figure 17). The bottom of the polyhedron was defined by fitting a plane through the four atoms connecting the four feet of the cavitand to the bottom row of aromatic rings. The top of the pocket polyhedron was determined by fitting a plane through the (diphenyl ether) eight oxygen atoms on the rim of the cavitand pocket. The average positions of the atoms making up the bottom and top planes of host **1** are illustrated in Supporting Figure 17. The remaining four planes making up the sides of the hexahedron were determined by fitting a plane through the average position of the two (diphenyl ether) oxygens that connect a single benzoic acid moiety on the rim to the two nearest carbons at the bottom of the pocket the define the bottom bounding plane. A water was considered to be within the cavitand pocket if it was within the constructed hexahedron. The four-fold C_4-axis of rotational symmetry for the cavitand is defined by the line passing though the bottom and top dummy atoms illustrated in Supporting Figure 17.

Cavitand partial molar volumes were determined as the average simulation box volume of the system with a single cavitand with its counterions and water, less that of pure water with the same number of waters:

$$\overline{v} = \langle V \rangle_{\substack{host+ \\ water}} - \lambda \langle V \rangle_{water},$$

which approximates the partial molar derivative as a finite difference with the pressure, temperature, and number of waters held fixed. The averages $\langle V \rangle_{\substack{host+ \\ water}}$ and $\langle V \rangle_{water}$ correspond to the mean simulation volumes with and without the added host. The volume of the pure water simulations was scaled by the factor $\lambda = N_{\substack{w,host+ \\ water}} / N_{w,water}$ to correct for differences in the number of waters in the simulation with and without the added host. This host volumes appearing in this expression were sorted based on the number of waters in the cavitand pocket to determine the partial molar volume on the basis of the pocket hydration state.

Additional information on the molecular simulations is provided in Section 3 of the Supporting Information.

Isothermal calorimetry measurements. ITC experiments were performed using a VP-ITC MicroCalorimeter from Microcal, USA. Curve fitting of the binding isotherms were processed using ORIGIN 7.0. Titrations were carried out in 50 mM phosphate buffer (pH = 11.6) at 25, 28, 32, 36, and 40˚C. Full details, including the injection volumes used for each titration and host and guest concentrations, are detailed in Section 4 of the Supporting Information.

References

42. Abraham, M. J., Murtola T., Schulz R., Páll S., Smith J. C., Hess B. & Lindahl E. GROMACS: High performance molecular simulations through multi-level parallelism from laptops to supercomputers. *SoftwareX* **1-2**, 19-25 (2015).

43. Horn, H. W., Swope W. C., Pitera J. W., Madura J. D., Dick T. J., Hura G. L. & Head-Gordon T. Development of an improved four-site water model for biomolecular simulations: TIP4P-Ew. *J. Chem. Phys.* **120**, 9665-9678 (2004).

44. Wang, J. M., Wolf R. M., Caldwell J. W., Kollman P. A. & Case D. A. Development and testing of a general amber force field. *J. Comput. Chem.* **25**, 1157-1174 (2004).

45. Jakalian, A., Bush B. L., Jack D. B. & Bayly C. I. Fast, efficient generation of high-quality atomic charges. AM1-BCC model: I. Method. *J. Comput. Chem.* **21**, 132-146 (2000).

46. Ewell, J., Gibb B. C. & Rick S. W. Water inside a hydrophobic cavitand molecule. *J. Phys. Chem. B* **112**, 10272-10279 (2008).

47. Darden, T., York D. & Pedersen L. Particle mesh Ewald - An N.log(N) method for Ewald Sums in large systems. *J. Chem. Phys.* **98**, 10089-10092 (1993).

48. Nosé, S. A unified formulation of the constant temperature molecular-dynamics methods. *J. Chem. Phys.* **81**, 511-519 (1984).

49. Hoover, W. G. Canonical dynamics: Equilibrium phase-space distributions. *Phys. Rev. A* **31**, 1695-1697 (1985).

50. Parrinello, M. & Rahman A. Polymophic transitions in single-crystals - A new molecular-dynamics method. *J. Appl. Phys.* **52**, 7182-7190 (1981).

51. Hess, B., Bekker H., Berendsen H. J. C. & Fraaije J. LINCS: A linear constraint solver for molecular simulations. *J. Comput. Chem.* **18**, 1463-1472 (1997).

52. Miyamoto, S. & Kollman P. A. SETTLE - An analytical version of the shake and rattle algorithm for rigid water models. *J. Comput. Chem.* **13**, 952-962 (1992).

Data Availability

The results appearing in Figures 2-4 are provided in Source Data Microsoft Excel spreadsheets linked in the HTML version of the paper. Data from Supporting Figures 16, 18, 19 are provided in a Microsoft Excel spreadsheet in the **Supporting Data**. In addition, we provide GROMACS topology and Gromos87 files for hosts **1**-**3** in a .zip file in the **Supporting Data**. Additional information supporting the findings of this study are available from the corresponding author upon reasonable request.

Code Availability

Not applicable.

a)

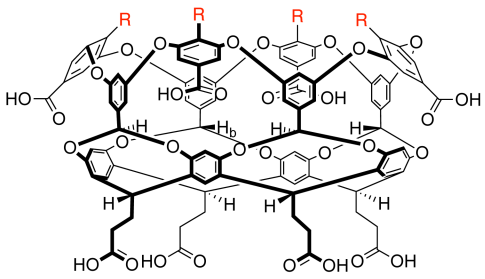

1: R = H (OA)
2: R = Me (TEMOA)

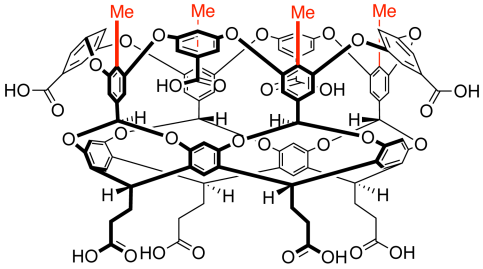

3 (TEXMOA)

b)

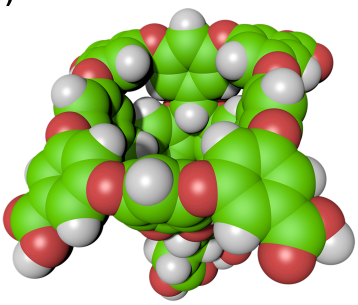

OA **1**

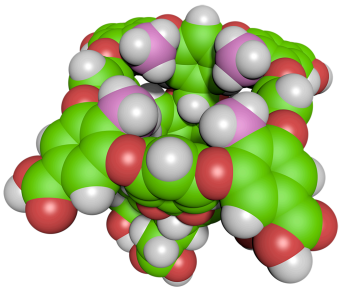

TEMOA **2**

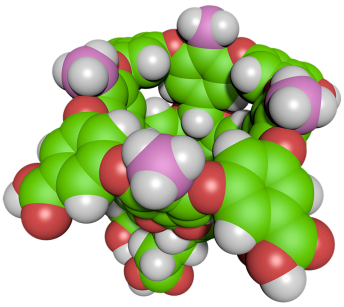

TEXMOA **3**

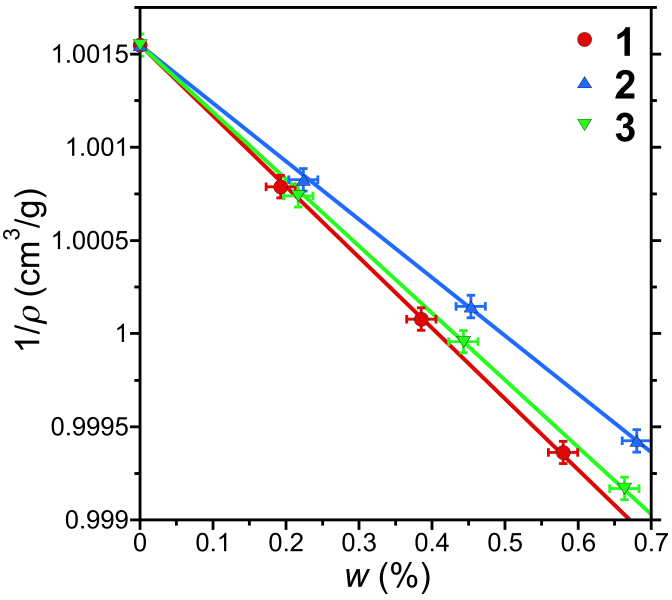
1
2
3
1.0015
1.001
1.0005
1
0.9995
0.999
0
0.1
0.2
0.3
0.4
0.5
0.6
0.7
1/ρ (cm3/g)
w (%)

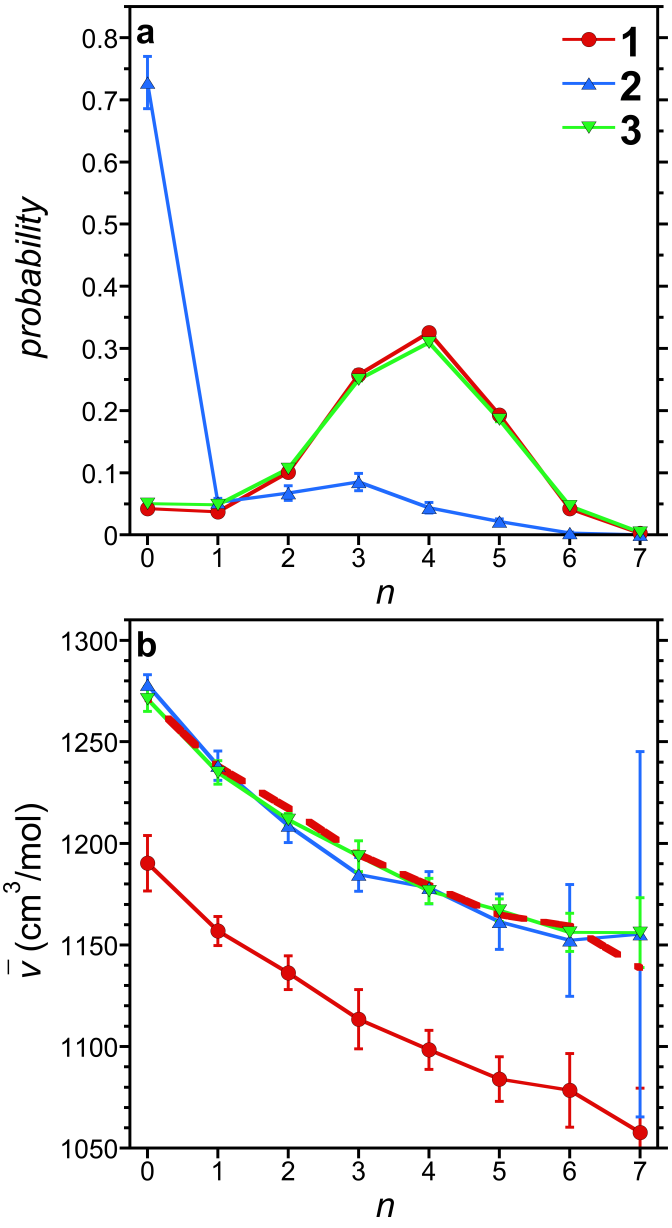
a
1
2
3
probability
n
b
$\bar{v}$ (cm^3/mol)
n

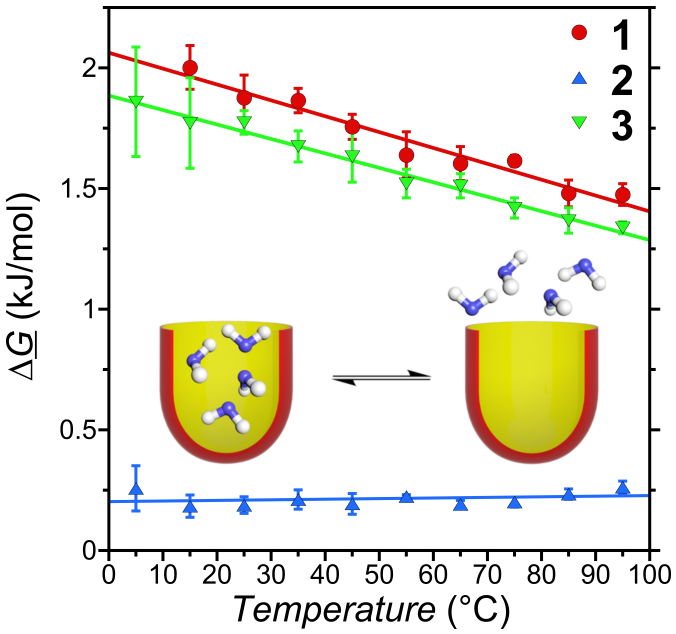
1
2
3
ΔG (kJ/mol)
0
0.5
1
1.5
2
0
10
20
30
40
50
60
70
80
90
100
Temperature (°C)